

# PREDICTION OF THE RESONANCE CONDITION OF METAMATERIAL EMITTERS AND ABSORBERS USING LC CIRCUIT MODEL

Atsushi Sakurai,<sup>1,2</sup> Bo Zhao,<sup>1</sup> Zhuomin M. Zhang<sup>1\*</sup>

<sup>1</sup>School of Mechanical Engineering, Georgia Institute of Technology, Atlanta, GA 30332, USA

<sup>2</sup>Niigata University, 8050, Ikarashi 2-no-cho, Niigata, 950-2181, Japan

## ABSTRACT

Electromagnetic metamaterial emitters and absorbers rely on a variety of electromagnetic resonances (i.e., polaritons) with different metallic nano/microstructured patterns such as strips, squares, circular disks, crosses, and square rings. A unique mechanism exists for different structures with various metallic patterns due to the similarity of the configuration. Thus, we explore a unified model which can greatly simplify the design process of these nano/microstructures. In the present study, an inductor-capacitor (LC) circuit model is used to predict the magnetic resonance conditions or magnetic polaritons (MPs) for metamaterial emitters and absorbers with different shapes. By suitably adjusting some of the parameters, the LC circuit model can reasonably predict the resonance conditions for published experimental results as well as rigorous electromagnetic wave simulations for the fundamental MP mode regardless of the shape of the metallic patterns. This study may facilitate the initial design of metamaterial emitters and absorbers.

**KEY WORDS:** Emitters and absorbers, LC circuit model, magnetic polariton, metamaterial

## 1. INTRODUCTION

Electromagnetic metamaterials have drawn much attention lately not only for their exotic optical and electromagnetic characteristics, but also for their potential applications such as optical cloaking [1], negative refraction [2], and perfect lenses [3]. Most electromagnetic metamaterials consist of periodic nano/microstructured elements. For example, the structure proposed by Pendry et al. [4] is composed of periodic “artificial atoms” that could exhibit exotic electromagnetic behaviours. These characteristics are usually impossible to achieve with naturally existing materials [5]. In addition to optical imaging and cloaking applications, these materials may be good candidates for perfect emitters and absorbers of thermal radiation at certain spectral band(s). A typical type of thermal emitters or absorbers is made of metal-insulator-metal configuration, which consists of three regions: a periodic pattern of nanostructures as the top region, a dielectric thin film as the middle region, and another metal layer as the bottom region that is thick enough for it to be considered opaque to thermal radiation [6]. When a time-varying magnetic field is introduced to the structure, oscillating antiparallel currents are induced that creates magnetic resonances, i.e., magnetic polaritons (MPs). MPs have been used to control radiative properties of thermal emitters and absorbers [7-14], which have wide practical application areas such as wavelength-selective thermal emitters and absorbers, thermophotovoltaics [15-21], and biosensors [22]. These emitters and absorbers can be applied not only near to the infrared region, but also gigahertz to terahertz regions [23].

Since the first experimental demonstration in 2008 [24], many electromagnetic metamaterial emitters and absorbers with a variety of top metallic patterns has been proposed for application in three major different spectral regions: visible and near-infrared (0.4 - 2.0  $\mu\text{m}$ ), mid-infrared (2.0 - 30  $\mu\text{m}$ ), and terahertz or far-infrared (30 - 1000  $\mu\text{m}$ ). Typical patterns include a) strips [13], b) squares [25-27], c) crosses [30], d)

\*Corresponding Author: zhuomin.zhang@me.gatech.edu

circular disks [22, 28-29], and e) square rings [31]. A unit cell of period  $\Lambda$  in both the  $x$  and  $y$  directions is shown in Fig. 1 for each case with a top metallic pattern over a metallic ground plate, separated by a dielectric spacer of thickness  $d$ . The geometry of the patterned structure is described by the characteristic lengths  $w$  and  $l$ , and thickness  $h$ . For circular disks, characteristic length  $w$  is equal to the diameter of disk. Different theories have been used to explain the resonances, such as transmission line theory [32], interference theory [33], and coupled mode theory [34]. Although the predictions of these theories show good agreement with simulation and/or experiments for specific structures, a unique mechanism may exist for different structures with various metallic patterns due to the similarity of the configuration. Thus, it is interesting to explore the possibility of a unified model, which can greatly simplify the design process of these nano/microstructures. Since antiparallel currents are induced in the top metallic structure and bottom metallic film under an incident time-varying magnetic field [12], magnetic coupling seems to be the most plausible explanation for the resonance phenomena in these structures. Therefore, a simple LC circuit model [35] may be able to predict the resonance frequency (wavelength), which is one of the most important design parameters, of structures with different shapes of metallic toppings.

In the present study, an LC circuit model is used to predict the magnetic resonance condition for the electromagnetic metamaterial emitters and absorbers. The applicability of the LC circuit model is explored over a large wavelength range and for various geometric patterns by comparison with published experimental results as well as full-wave numerical simulations. Furthermore, a modified LC circuit model is proposed specifically for the square-ring pattern shown in Fig. 1e. The electric and magnetic field distributions are calculated using a finite-difference time-domain (FDTD) method to illustrate the magnetic responses and their relative strength in different structures.

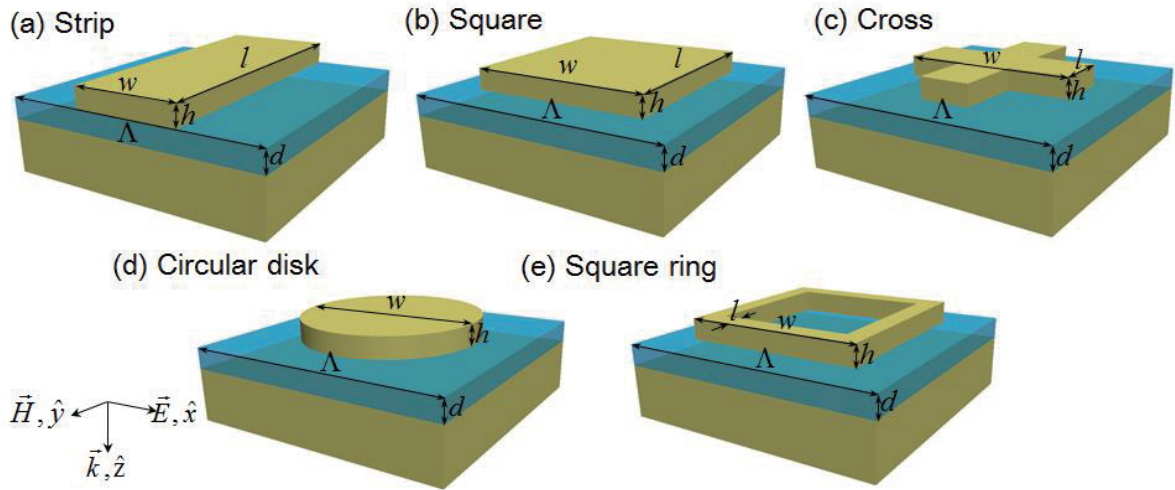


**Fig. 1** Schematic of typical electromagnetic metamaterial emitters and absorbers. Unit cells are shown as different top gold patterns over a ground plate separated by a dielectric spacer ( $\text{Al}_2\text{O}_3$ ): (a) strip, (b) square, (c) cross, (d) circular disk, and (e) square ring.

## 2. LC CIRCUIT MODEL AND RIGOROUS NUMERICAL SIMULATION

**2.1 LC circuit model** The LC circuit model as shown in Fig. 2 has been successfully applied to predict the magnetic resonance conditions for nano/microstructures with metal-dielectric-metal configuration [7-14]. When MPs are excited, magnetic field is strongly confined between the top metallic structure and the bottom metallic film. Hence, the considered structure can be assumed to be metal strip pairs although a thick bottom metallic film is used. The magnetic inductance or mutual inductance ( $L_m$ ), which is originated from the magnetic energy stored in the dielectric spacer of distance  $d$  between the two parallel plates, has the form [10],

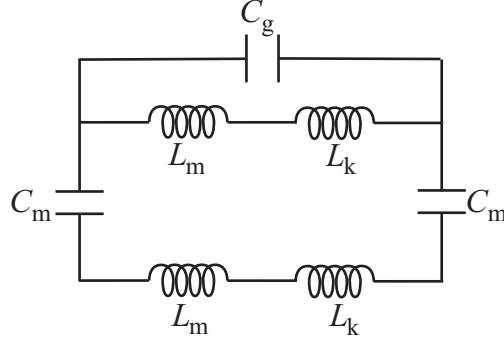


**Fig. 2** Equivalent LC circuit model for the fundamental MP mode.

$$L_m = 0.5\mu_0 \frac{wd}{l} \quad (1)$$

where  $\mu_0$  is the permeability of vacuum. The kinetic inductance, which is originated from the kinetic energy of the electrons inside the metal, can be expressed as [10,14]

$$L_k = -\frac{w}{\varepsilon_0 \omega^2 l \delta} \frac{\varepsilon'}{(\varepsilon'^2 + \varepsilon''^2)} \quad (2)$$

where  $\varepsilon'$  and  $\varepsilon''$  are the real and imaginary parts of the dielectric function ( $\varepsilon$ ) of the metal, respectively, and  $\delta = \lambda/2\pi\kappa$  is the penetration depth of the electric field, with  $\kappa$  being the extinction coefficient. Note that the field penetration depth is twice the penetration depth of the radiation power [14]. The dielectric that separates top metal structure and the ground plate serves as a capacitor whose capacitance can be expressed as

$$C_m = c' \varepsilon_d \varepsilon_0 \frac{wl}{d} \quad (3)$$

where  $c'$  is a numerical factor to take account of the fringe effect or non-uniform charge distribution along the surfaces of capacitor. Another capacitor is formed by the air gap between neighboring top metal structures and is given by

$$C_g = \varepsilon_0 \frac{hl}{\Lambda - w} \quad (4)$$

The resonance condition for the fundamental MP mode can be obtained by zeroing the total impedance

$$Z_{\text{tot}}(\omega) = \frac{L_m + L_k}{1 - \omega^2 C_g (L_m + L_k)} - \frac{2}{\omega^2 C_m} + L_k + L_m \quad (5)$$

Since the penetration depth and dielectric function are wavelength-dependent, the resonance condition is solved implicitly. Note that the capacitance is proportional to  $l$  and the inductance is inversely proportional to  $l$ , thus, the solution of  $Z_{\text{tot}}(\omega) = 0$  is independent of  $l$ .

**2.2 Full-wave numerical simulation** In the present study, numerical simulations are performed with the Lumerical FDTD Solution software package. A unit cell of the considered structure is modeled with periodic boundary conditions along the  $x$  and  $y$  directions. Perfectly matched layers are used along the propagation direction of electromagnetic waves ( $z$  direction). Plane electromagnetic waves were incident to the unit cell from above the structure shown in Fig. 1. The reflected waves are collected with a frequency-domain monitor placed above the structure. Only the transverse magnetic (TM) wave is considered for which MPs can be excited by the  $y$  component of the magnetic field. For transverse electric (TE) waves, MPs are excited by the  $x$  component of the magnetic field. However, the reflectance would be the same for both TE and TM waves due to symmetry. According to Kirchhoff's law [5], the spectral-directional emittance is equal to the spectral-directional absorptance, which is one minus the reflectance providing that the bottom metal layer is opaque. The normal specular reflectance is calculated from the FDTD, and the surface roughness effect is not considered in the calculation. Angular dependence of emittance is expected to be weak because the  $y$  component of the magnetic field, which excites the resonance, does not change for the TM wave when the incidence angle changes [12]. All the simulations in this paper are performed in three-dimensional computational domain using non-uniform cubic mesh with a minimum mesh size of 10 nm. The parameters used in the simulation are listed in Table 1. The geometric parameters are fixed as follows:  $\Lambda = 3.2 \mu\text{m}$ ,  $h = 100 \text{ nm}$ ,  $w = 1.7 \mu\text{m}$ , and  $d = 140 \text{ nm}$ . Alumina ( $\text{Al}_2\text{O}_3$ ) is chosen for a dielectric spacer and gold is chosen as metal. The dielectric functions of alumina and gold are obtained with the tabulated values from Palik [36]. Here, the refractive index of alumina is assumed to be constant in the considered spectral region and set to  $n_d = 1.57$ .

**Table 1** Parameters used in the simulations

Period	$\Lambda [\mu\text{m}]$	3.2
Thickness of metal	$h [\text{nm}]$	100
Thickness of dielectric spacer	$d [\text{nm}]$	140
Characteristic length	$w [\mu\text{m}]$	1.7
$y$ -directional length (Strip)	$l [\mu\text{m}]$	3.2
$y$ -directional length (Square)	$l [\mu\text{m}]$	1.7
$y$ -directional length (Cross)	$l [\mu\text{m}]$	0.5

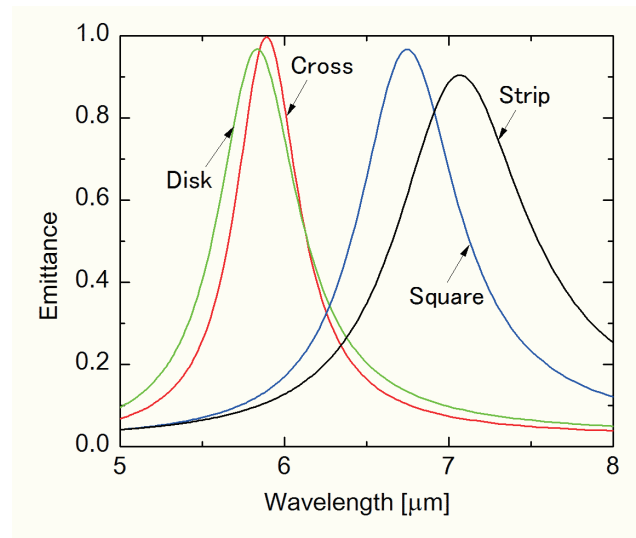


**Fig. 3** Normal emittance of the metamaterial structures with different top metallic pattern.

Figure 3 shows the simulated normal emittance spectra of the metamaterial structures with different top patterns. The emittance peaks of circular disk, cross, square, and strip patterns are located at 5.83, 5.89, 6.74, and 7.08  $\mu\text{m}$ , respectively. These emittance peaks are due to the coupling of the magnetic resonance or MPs inside the micro/nanostructure with external electromagnetic waves. The prediction of resonant wavelength by the LC circuit model with two parallel strips is 6.49  $\mu\text{m}$  when  $c' = 0.22$  is used. Note that  $c'$  used in the capacitance model does not have to be the same for different cases since the charge distributions are different. The surface charge distribution depends on the geometry, so the capacitance may not be equal for different top patterns. Therefore,  $c'$  used in Eq. (3) may be taken as an adjustable parameter to fit the resonance peaks of different structures. Specifically, value of  $c'$  obtained this way is 0.176, 0.182, 0.238, and 0.262 the patterns with circular disks, crosses, squares, and strips. These values are in reasonable range considering the simplicity of the LC model without considering the detailed coupling for various geometries. Clearly, the LC circuit model can be reasonably applied to various patterns of metamaterial emitters and absorbers. Further understanding of the magnetic resonance in different structures can be gained by examining the field profiles.

When the MP is excited, the magnetic field is strongly enhanced in the dielectric layer sandwiched between the top metallic pattern and ground plate, as shown in Fig. 4. The color contour indicates the squared magnetic field (normalized to the incident magnetic field), and the arrows indicate the electric field vectors in the cross-section along the  $x$ - $z$  plane as shown in Fig. 4a with the cross pattern. Clearly, an electric current loop is formed and strong magnetic field is confined in the dielectric layer. The coupling between the cross pattern and ground plate are the strongest among these patterns. This can be further verified by considering the field profile in the  $x$ - $y$  plane. Figure 5 shows the magnetic field profile at the resonant wavelength in the middle of the dielectric spacer (as illustrated by the cross-section in Fig. 5a). The color contour in Figs. 5b-5e indicates the squared magnetic field. The strongest magnetic field enhancement and localization occur in the cross pattern as shown in Fig. 5e. The magnetic field is also enhanced for the strip pattern. However, the relative magnitude of strip pattern is the weakest of the four metallic patterns. Also, it can be seen that the magnetic field is distributed widely under the strip pattern. The resulting absorptance or emittance is similar for all structures with the cross pattern being the highest (close to unity) and then circular disk, square, and strip patterns in decreasing order. Figs. 4 and 5 clearly show that MPs are excited in all four structures. The resonant emittance spectra depend on the top metallic patterns, which yield different enhanced magnetic field profiles.

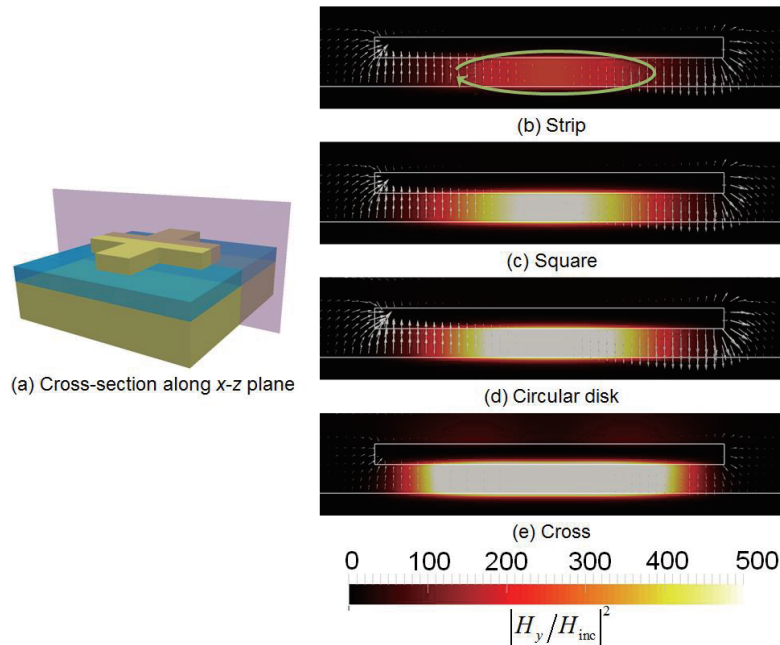


**Fig. 4** Electromagnetic field profile at the resonant wavelength. The color contour shows the relative magnitude of the  $y$  component of the magnetic field. The vectors show the direction and magnitude of the electric field: (a) Three-dimensional schematic view of metamaterial with a cross pattern and the cross-section along the  $x$ - $z$  plane, (b) strip, (c) square, (d) circular disk, and (e) cross pattern.



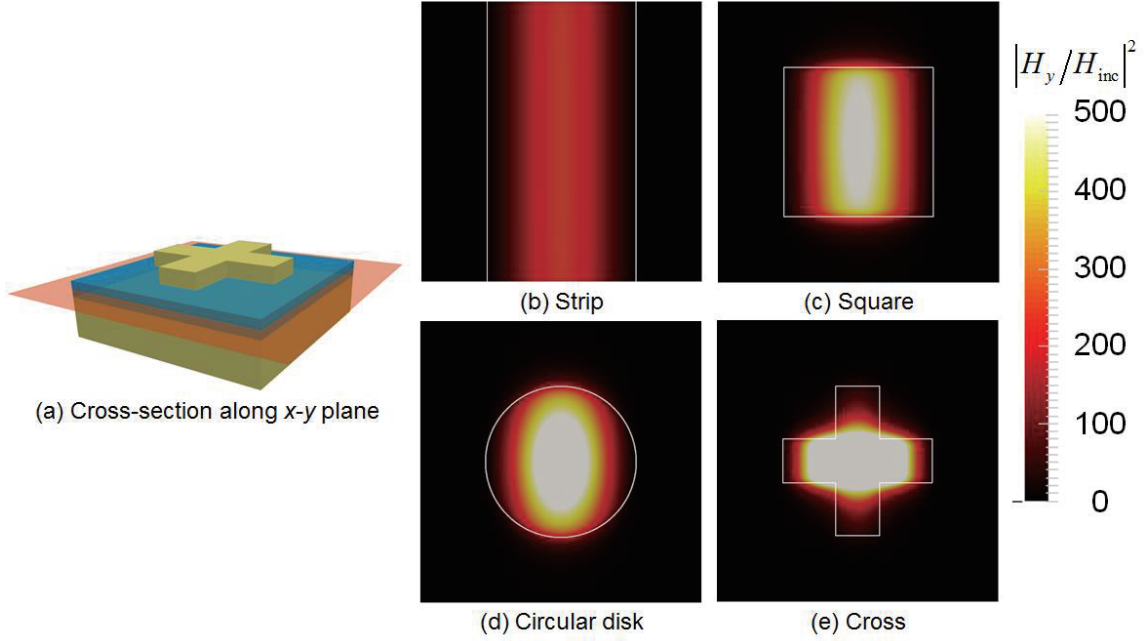


**Fig. 5** Magnetic field profile at the resonant wavelength. The color contour shows the relative magnitude of the  $y$  component of the magnetic field: (a) Three-dimensional schematic view of metamaterial with a cross pattern and the cross-section along the  $x$ - $y$  plane, (b) strip, (c) square, (d) circular disk, and (e) cross pattern.

### 3. COMPARISON WITH PUBLISHED EXPERIMENTAL DATA

In this section, the applicability of the LC circuit model is explored by comparison with published experimental results over a wide wavelength range and for various patterns. Table 2 shows the design parameters obtained from published experimental results. The resonance wavelengths obtained from experiments  $\lambda_{R,exp}$  and from the LC circuit model  $\lambda_{R,LC}$  are listed in Table 3 for the corresponding cases and widths. The parameters calculated from the LC circuit model, such as the penetration depth, mutual and kinetic inductances, and capacitances are also shown in the table. For simplicity, the value of  $c'$  used in the LC model prediction is fixed at 0.22 for all the calculations.

For the strip pattern, comparison is made with the experiments for a 1D gold grating microstructure [13]. Patterns 1 and 2 have different strip width ( $w = 2.5 \mu\text{m}$  and  $3.5 \mu\text{m}$ ) and Au grating height ( $h = 180 \text{ nm}$  and  $170 \text{ nm}$ ). The experimental peak locations are at  $7.10 \mu\text{m}$  and  $7.75 \mu\text{m}$ , respectively. The predictions by the LC circuit model are at  $6.76 \mu\text{m}$  and  $7.48 \mu\text{m}$ , respectively. For the square pattern, experimental results from the works of Hendrikson et al. [25] and Bouchon et al. [26] are considered as Square-1 and Square-2, respectively. Multiple squares with different sizes were used as top patterns to create broadband absorptance in these studies. Square-1 has two characteristic widths ( $w = 0.815 \mu\text{m}$  and  $0.865 \mu\text{m}$ ), while Square-2 has four characteristic widths ( $w = 1.64 \mu\text{m}$ ,  $1.78 \mu\text{m}$ ,  $1.91 \mu\text{m}$ , and  $2.07 \mu\text{m}$ ). As shown in the table, the prediction by the LC circuit model agrees reasonably well with the experimental resonant wavelengths. Alaei et al. [27] (Square-3) explored an extreme coupling phenomenon inside a thin dielectric spacer only a few nanometers. Even though the magnitude of inductances and capacitances are very different compared to others, the LC circuit model can still reasonably predict the experimental resonant wavelength. Note that different dielectric materials were used as the dielectric spacers. The optical constants of  $\text{SiO}_2$  and  $\text{Al}_2\text{O}_3$  are taken from Palik [36] and those of the rest are assumed constant as listed in Table 2.

Liu et al. [22] demonstrated gold circular disks for application to bio-sensors (Disk-1). The height of the gold disk is  $20 \text{ nm}$ , which is smaller than the penetration depth. Therefore, the height of gold disks is used in place of

the penetration depth in the LC circuit model. The experimental resonant wavelength is 1.60  $\mu\text{m}$ , which agrees well with the LC circuit model prediction of 1.64  $\mu\text{m}$ . The cases represented by Disk-2 and Disk-3 are adopted from Puscasu et al. [28] and Cheng et al. [29], respectively. Note that aluminum and silver were used in these studies. The optical constants of silver and gold are also taken from Palik [36] in the LC model, and the optical constants of aluminum are obtained by a Drude model by fitting to Palik [36]. Again, the predictions by LC circuit model are in reasonable agreement with the experimental resonant wavelengths.

**Table 2.** Geometric parameters and materials based on published experimental research.

Case	Authors	Metal	Dielectric spacer	$\Lambda$ [ $\mu\text{m}$ ]	$h$ [nm]	$d$ [nm]	$w$ [ $\mu\text{m}$ ]
Strip	Wang and Zhang <sup>[13]</sup>	Au <sup>[36]</sup>	SiO <sub>2</sub> <sup>[36]</sup>	7.00	170 and 180	200	2.5 and 3.5
Square-1	Hendrikson et al. <sup>[25]</sup>	Au <sup>[37]</sup>	MgF <sub>2</sub> ( $n_d = 1.36$ )	2.10	55	75	0.815 and 0.865
Square-2	Bouchon et al. <sup>[26]</sup>	Au <sup>[26]</sup>	ZnS ( $n_d = 2.20$ )	5.30	50	290	1.64, 1.78, 1.91, and 2.07
Square-3	Alaee et al. <sup>[27]</sup>	Au <sup>[38]</sup>	SiO <sub>2</sub> <sup>[27]</sup> ( $n_d = 1.50$ )	0.25	30	3	0.195
Disk-1	Liu et al. <sup>[22]</sup>	Au <sup>[22]</sup>	MgF <sub>2</sub> ( $n_d = 1.36$ )	0.60	20	30	0.352
Disk-2	Puscasu et al. <sup>[28]</sup>	Al <sup>[28]</sup>	SiO <sub>2</sub> <sup>[36]</sup>	3.40	100	100	1.70
Disk-3	Cheng et al. <sup>[29]</sup>	Ag <sup>[36]</sup>	SiO <sub>2</sub> <sup>[36]</sup>	1.50	100	80	1.00
Cross	Liu et al. <sup>[30]</sup>	Au <sup>[39]</sup>	Al <sub>2</sub> O <sub>3</sub> <sup>[36]</sup>	3.20	100	200	1.70
Ring <sup>[*]</sup>	Ma et al. <sup>[31]</sup>	Au <sup>[31]</sup>	Polymer ( $n_d = 1.55$ )	28.0	220	4000	11 and 19

[\*] Width of the metal strip  $l = 0.5$  [ $\mu\text{m}$ ]

**Table 3.** Comparison of the resonance conditions for different cases and the physical parameters calculated for the LC circuit model.

Case	$w$ [ $\mu\text{m}$ ]	$\lambda_{R,\text{exp}}$ [ $\mu\text{m}$ ]	$\lambda_{R,\text{LC}}$ [ $\mu\text{m}$ ]	$\delta$ [nm]	$L_m$ [H]	$L_k$ [H]	$C_m$ [F]	$C_g$ [F]
Strip	2.5	7.10	6.76	26.6	$3.14 \times 10^{-19}$	$7.77 \times 10^{-20}$	$3.27 \times 10^{-11}$	$3.54 \times 10^{-13}$
	3.5	7.75	7.48	27.1	$4.40 \times 10^{-19}$	$1.09 \times 10^{-19}$	$2.85 \times 10^{-11}$	$4.30 \times 10^{-13}$
Square-1	0.815	3.36	2.99	25.4	$4.71 \times 10^{-14}$	$3.11 \times 10^{-14}$	$3.18 \times 10^{-17}$	$3.09 \times 10^{-19}$
	0.865	3.55	3.18	25.6	$4.71 \times 10^{-14}$	$3.13 \times 10^{-14}$	$3.58 \times 10^{-17}$	$3.41 \times 10^{-19}$
Square-2	1.64	7.58	8.14	25.8	$1.82 \times 10^{-13}$	$3.11 \times 10^{-14}$	$8.74 \times 10^{-17}$	$1.98 \times 10^{-19}$
	1.78	8.17	8.83	25.9	$1.82 \times 10^{-13}$	$3.10 \times 10^{-14}$	$1.03 \times 10^{-16}$	$2.24 \times 10^{-19}$
	1.91	8.90	9.48	26.0	$1.82 \times 10^{-13}$	$3.09 \times 10^{-14}$	$1.19 \times 10^{-16}$	$2.49 \times 10^{-19}$
	2.07	9.47	10.3	26.1	$1.82 \times 10^{-13}$	$3.07 \times 10^{-14}$	$1.39 \times 10^{-16}$	$2.84 \times 10^{-19}$
Square-3	0.195	2.25	2.60	26.0	$1.89 \times 10^{-15}$	$3.22 \times 10^{-14}$	$5.56 \times 10^{-17}$	$9.42 \times 10^{-19}$
Disk-1	0.352	1.60	1.64	20.0	$1.89 \times 10^{-14}$	$3.03 \times 10^{-14}$	$1.53 \times 10^{-17}$	$2.51 \times 10^{-19}$
Disk-2	1.70	5.70	5.76	30.0	$6.28 \times 10^{-14}$	$3.60 \times 10^{-14}$	$9.40 \times 10^{-17}$	$8.85 \times 10^{-19}$
Disk-3	1.00	3.50	3.79	26.2	$5.03 \times 10^{-14}$	$3.23 \times 10^{-14}$	$4.81 \times 10^{-17}$	$1.77 \times 10^{-18}$
Cross	1.70	5.80	5.93	22.1	$4.27 \times 10^{-13}$	$9.32 \times 10^{-14}$	$1.89 \times 10^{-17}$	$2.95 \times 10^{-19}$
Ring	11.0	57.0	62.2	36.3	$2.77 \times 10^{-11}$	0.0	$3.94 \times 10^{-17}$	$1.15 \times 10^{-19}$
	19.0	111	109	48.0	$4.78 \times 10^{-11}$	0.0	$7.00 \times 10^{-17}$	$2.16 \times 10^{-19}$

For the case denoted as Cross-1, the pattern was experimentally demonstrated by Liu et al. [30]. They experimentally realized a narrow band mid-infrared thermal emitter which consists of gold cross and a ground gold plate. The experimental resonant wavelength is  $5.80\ \mu\text{m}$ , and the prediction by LC circuit model is  $5.93\ \mu\text{m}$ . Therefore, the prediction by the LC circuit model agrees well with the experimental result. It can be clearly seen that magnetic polaritons mainly depend on the characteristic width (i.e., the  $x$  directional width,  $w$ ) of the top metal structure regardless of the geometric differences.

The LC circuit model provides an effective way to locate the fundamental mode of MPs, namely, the resonant wavelength. However, the simple LC circuit model cannot provide any information on the bandwidth or magnitude of the peak. Also, the accuracy of the LC circuit model is subject to the approximation of  $c'$  due to the nonuniform charge distribution in the metal. Besides, the penetration depth used in Eq. (2) is merely an effective average that may not precisely model the actual kinetic inductance. Since a strong field coupling occurs in the near-infrared range for small metal height  $h$  and/or small dielectric layer thickness  $d$  (below about  $10\ \text{nm}$ ), the formulation of penetration depth becomes important since the kinetic inductance  $L_k$  is larger than or comparable with the mutual inductance  $L_m$  [14]. On the other hand, in some of the previous studies [7-13], the penetration depth  $\delta = \lambda/4\pi\kappa$  seems to work well. For mid-infrared and far-infrared regions, there is little difference between the prediction using different penetration depth values since  $L_k \ll L_m$ .

#### 4. PREDICTION FOR SQUARE-RING PATTERN

Ma et al. [31] experimentally demonstrated resonance absorption by the square-ring pattern, as shown in Fig. 1e, in terahertz wavelengths. At such low frequencies, the kinetic inductance is much smaller than the mutual inductance and can be neglected. The current and charge distributions of square-ring pattern are different from those of the other structures. The current flows in the two strips parallel to  $x$ . The mutual inductance may be expressed as follows:

$$L_m = 0.5\mu_0 \frac{wd}{2l} \quad (6)$$

where  $l$  as the width of each strip as defined in Fig. 1e. The external TM wave excites antiparallel currents due to the magnetic resonance along the metal in  $x$  direction with the same mechanism as other structures; on the other hand, the strips parallel to the  $y$  direction support charge accumulation and oscillation. Therefore, additional capacitance needs to be added to the capacitance model, and the modified total capacitance is expressed as follows:

$$C_m = c'\epsilon_d\epsilon_0 \frac{w(2l)}{d} + \epsilon_d\epsilon_0 \frac{l(w-2l)}{d} \quad (7)$$

Here, the first term on the right side represents parallel-plate capacitance for the two strips parallel to the  $x$  direction with  $c' = 0.22$  as before, and the second term represent parallel-plate capacitance of the end strip parallel to the  $y$  direction (subtracted by the overlapping corner region).

In the experimental study by Ma et al. [31], gold square-ring patterns were used with the characteristic lengths  $w = 11\ \mu\text{m}$  and  $19\ \mu\text{m}$ . In this wavelength region, gold can be considered to be a perfect conductor. Hence, the Hagen-Rubben equation  $\epsilon'' = i\sigma/\omega\epsilon_0$  is used for its dielectric function [5]. The experimental peak locations for ring pattern with  $w = 11\ \mu\text{m}$  and  $19\ \mu\text{m}$  are  $57\ \mu\text{m}$  and  $111\ \mu\text{m}$ , respectively, and these predicted by the modified LC circuit model are  $62.2\ \mu\text{m}$  and  $109\ \mu\text{m}$ , respectively. Therefore, the modified LC circuit model can reasonably predict the resonance condition for the square-ring pattern. These findings may be useful for a unified explanation of the various resonances in different structures.



## 5. CONCLUSIONS

The simple LC circuit model can reasonably predict the resonance conditions for the fundamental MP mode regardless of the top metallic patterns. Even with different patterns, the resonances within the structure share the same excitation mechanism. The resonance wavelength of MPs mainly depends on the characteristic width (i.e.,  $x$ -directional width perpendicular to the magnetic field). The resonance condition predicted by the LC circuit model agrees reasonably well with that obtained from the FDTD simulations as well as the published experimental data. The LC circuit model can also be modified to predict the resonant wavelength for the square-ring pattern. This study suggests a unified way of predicting the resonant conditions for various metamaterial structures, and will facilitate the simple and user-friendly initial design of metamaterial emitters and absorbers.

## ACKNOWLEDGMENTS

This work was supported by the National Science Foundation (CBET-1235975). The authors would like to thank Dr. Junming Zhao for valuable comments and Mr. Xianglei Liu for help in the FDTD simulation.

## NOMENCLATURE

$C_m$	Capacitance of dielectric spacer	(F)	$\delta$	Penetration depth	(nm)
$C_g$	Capacitance of air gap	(F)	$\epsilon_0$	Permittivity of vacuum	$(8.854 \times 10^{-12} \text{ F m}^{-1})$
$c'$	Numerical factor	(-)	$\epsilon$	Dielectric function of metal	(-)
$d$	Thickness of dielectric spacer	(nm)	$\epsilon_d$	Dielectric function of dielectric spacer	(-)
$h$	Thickness of metal	(nm)	$\Lambda$	Period	( $\mu\text{m}$ )
$l$	Length	( $\mu\text{m}$ )	$\lambda$	Wavelength	( $\mu\text{m}$ )
$L_m$	Mutual inductance	(H)	$\lambda_{R,\text{exp}}$	Resonant wavelength from experiment	( $\mu\text{m}$ )
$L_k$	Kinetic inductance	(H)	$\lambda_{R,\text{LC}}$	Resonant wavelength from LC circuit model	( $\mu\text{m}$ )
$n_d$	Refractive index of dielectric spacer	(-)	$\mu_0$	Permeability of vacuum	$(4\pi \times 10^{-7} \text{ N A}^{-2})$
$w$	Characteristic length	( $\mu\text{m}$ )	$\sigma$	Electrical conductivity	(S/m)
$Z_{\text{tot}}$	Total impedance	( $\Omega$ )	$\omega$	Frequency	(Hz)

## REFERENCES

- [1] Schurig, D., Mock, J. J., Justice, B. J., Cummer, S. A., Pendry, J. B., Starr, A. F., and Smith, D. R., "Metamaterial electromagnetic cloak at microwave frequencies," *Science*, 314(5801), pp. 977-980, (2006).
- [2] Smith, D. R., Pendry, J. B., and Wiltshire, M. C. K., "Metamaterials and negative refractive index," *Science*, 305(5685), pp. 788-792, (2004).
- [3] Pendry, J. B., "Negative refraction makes a perfect lens," *Physical Review Letters*, 85(18), pp. 3966-3969, (2000).
- [4] Pendry, J. B., Holden, A. J., Robbins, D. J., and Stewart, W. J., "Magnetism from conductors and enhanced nonlinear phenomena," *IEEE Transactions on Microwave Theory and Techniques*, 47(11), pp. 2075-2084, (1999).
- [5] Zhang, Z. M., *Nano/Microscale Heat Transfer* (McGraw-Hill, New York, 2007).
- [6] Watts, C. M., Liu, X. L., and Padilla, W. J., "Metamaterial electromagnetic wave absorbers," *Advanced Materials*, 24(23), pp. OP98-OP120, (2012).
- [7] Lee, B. J., Wang, L. P., and Zhang, Z. M., "Coherent thermal emission by excitation of magnetic polaritons between periodic strips and a metallic film," *Optics Express*, 16(15), pp. 11328-11336, (2008).

- [8] Chen, Y. B., and Chen, C. J., "Interaction between the magnetic polariton and surface plasmon polariton," *Optics Communications*, 297, pp. 169-175, (2013).
- [9] Liu, X. L., Zhao, B., and Zhang, Z. M., "Wide-angle near infrared polarizer with extremely high extinction ratio," *Optics Express*, 21(9), pp. 10502-10510, (2013).
- [10] Wang, L. P., and Zhang, Z. M., "Phonon-mediated magnetic polaritons in the infrared region," *Optics Express*, 19(6), pp. A126-A135, (2011).
- [11] Wang, L. P., and Zhang, Z. M., "Wavelength-selective and diffuse emitter enhanced by magnetic polaritons for thermophotovoltaics," *Applied Physics Letters*, 100(6), p. 063902, (2012).
- [12] Zhao, B., Wang, L.P., Shuai, Y., and Zhang, Z. M., "Thermophotovoltaic emitters based on a two-dimensional grating/thin-film nanostructure," *International Journal of Heat and Mass Transfer*, 67, pp. 637-645, (2013).
- [13] Wang, L.P., and Zhang, Z.M., "Measurement of coherent thermal emission due to magnetic polaritons in subwavelength microstructures," *Journal of Heat Transfer*, 35, p. 091505, (2013).
- [14] Zhao, B., and Zhang, Z. M., "Study of magnetic polaritons in deep gratings for thermal emission control," *Journal of Quantitative Spectroscopy and Radiative Transfer*, in press.
- [15] Maruyama, S., Kashiwa, T., Yugami, H., and Esashi, M., "Thermal radiation from two-dimensionally confined modes in microcavities," *Applied Physics Letters*, 79(9), pp. 1393-1395, (2001).
- [16] Chester, D., Bermel, P., Joannopoulos, J. D., Soljacic, M., and Celanovic, I., "Design and global optimization of high-efficiency solar thermal systems with tungsten cermet," *Optics Express*, 19(10), pp. A245-A257, (2011).
- [17] Bermel, P., Ghebrebrhan, M., Chan, W., Yeng, Y. X., Araghchini, M., Hamam, R., Marton, C. H., Jensen, K. F., Soljacic, M., Joannopoulos, J. D., Johnson, S. G., and Celanovic, I., "Design and global optimization of high-efficiency thermophotovoltaic systems," *Optics Express*, 18(19), pp. A314-A334, (2010).
- [18] Sergeant, N. P., Agrawal, M., and Peumans, P., "High performance solar-selective absorbers using coated sub-wavelength gratings," *Optics Express*, 18(6), pp. 5525-5540, (2010).
- [19] Sergeant, N. P., Pincon, O., Agrawal, M., and Peumans, P., "Design of wide-angle solar-selective absorbers using aperiodic metal-dielectric stacks," *Optics Express*, 17(25), pp. 22800-22812, (2009).
- [20] Sakurai, A., Tanikawa, H., and Yamada, M., "Computational design for a wide-angle cermet-based solar selective absorber for high temperature applications," *Journal of Quantitative Spectroscopy and Radiative Transfer*, 132, pp. 80-89, (2014).
- [21] Sai, H., Kanamori, Y., and Yugami, H., "High-temperature resistive surface grating for spectral control of thermal radiation," *Applied Physics Letters*, 82(11), pp. 1685-1687, (2003).
- [22] Liu, N., Mesch, M., Weiss, T., Hentschel, M., and Giessen, H., "Infrared perfect absorber and its application as plasmonic sensor," *Nano Letters*, 10(7), pp. 2342-2348, (2010).
- [23] Landy, N. I., Bingham, C. M., Tyler, T., Jokerst, N., Smith, D. R., and Padilla, W. J., "Design, theory, and measurement of a polarization-insensitive absorber for terahertz imaging," *Physical Review B*, 79(12), p. 125104, (2009).
- [24] Landy, N. I., Sajuyigbe, S., Mock, J. J., Smith, D. R., and Padilla, W. J., "Perfect metamaterial absorber," *Physical Review Letters*, 100(20), p. 207402, (2008).
- [25] Hendrickson, J., Guo, J. P., Zhang, B. Y., Buchwald, W., and Soref, R., "Wideband perfect light absorber at midwave infrared using multiplexed metal structures," *Optics Letters*, 37(3), pp. 371-373, (2012).
- [26] Bouchon, P., Koechlin, C., Pardo, F., Haidar, R., and Pelouard, J. L., "Wideband omnidirectional infrared absorber with a patchwork of plasmonic nanoantennas," *Optics Letters*, 37(6), pp. 1038-1040, (2012).
- [27] Alae, R., Menzel, C., Huebner, U., Pshenay-Severin, E., Bin Hasan, S., Pertsch, T., Rockstuhl, C., and Lederer, F., "Deep-subwavelength plasmonic nanoresonators exploiting extreme coupling," *Nano Letters*, 13(8), pp. 3482-3486, (2013).
- [28] Puscasu, I., and Schaich, W. L., "Narrow-band, tunable infrared emission from arrays of microstrip patches," *Applied Physics Letters*, 92(23), p. 233102, (2008).
- [29] Cheng, C. W., Abbas, M. N., Chiu, C. W., Lai, K. T., Shih, M. H., and Chang, Y. C., "Wide-angle polarization independent infrared broadband absorbers based on metallic multi-sized disk arrays," *Optics Express*, 20(9), pp. 10376-10381, (2012).
- [30] Liu, X. L., Tyler, T., Starr, T., Starr, A. F., Jokerst, N. M., and Padilla, W. J., "Taming the Blackbody with Infrared Metamaterials as Selective Thermal Emitters," *Physical Review Letters*, 107(4), p. 045901, (2011).
- [31] Ma, Y., Chen, Q., Grant, J., Saha, S. C., Khalid, A., and Cumming, D. R. S., "A terahertz polarization insensitive dual band metamaterial absorber," *Optics Letters*, 36(6), pp. 945-947, (2011).
- [32] Engheta, N., "Circuits with light at nanoscales: Optical nanocircuits inspired by metamaterials," *Science*, 317(5845), pp. 1698-1702, (2007).
- [33] Chen, H.-T., "Interference theory of metamaterial perfect absorbers," *Optics Express*, 20(7), pp. 7165-7172, (2012).
- [34] Zhu, L. X., Sandhu, S., Otey, C., Fan, S. H., Sinclair, M. B., and Luk, T. S., "Temporal coupled mode theory for thermal emission from a single thermal emitter supporting either a single mode or an orthogonal set of modes," *Applied Physics Letters*, 102(10), p. 103104, (2013).
- [35] Zhou, J., Economou, E. N., Koschny, T., and Soukoulis, C. M., "Unifying approach to left-handed material design," *Optics Letters*, 31(24), pp. 3620-3622, (2006).
- [36] Handbook of Optical Constants of Solids, edited by E. D. Palik (Academic Press, San Diego, 1998).
- [37] Rakic, A. D., Djurisic, A. B., Elazar, J. M., and Majewski, M. L., "Optical properties of metallic films for vertical-cavity optoelectronic devices," *Applied Optics*, 37(22), pp. 5271-5283, (1998).
- [38] Johnson, P. B., and Christy, R. W., "Optical constants of noble metals," *Physical Review B*, 6(12), pp. 4370-4379, (1972).
- [39] Ordal, M. A., Long, L. L., Bell, R. J., Bell, S. E., Bell, R. R., Alexander, R. W., and Ward, C. A., "Optical-properties of the metals Al, Co, Cu, Au, Fe, Pb, Ni, Pd, Pt, Ag, Ti, and W in the infrared and far infrared," *Applied Optics*, 22(7), pp. 1099-1119, (1983).